# Stepwise deforestation during the Permian-Triassic boundary crisis linked to rising temperatures

Jiaqi Wu[1], Daoliang Chu[1], Genming Luo[1*], Paul B. Wignall[2], Thomas J. Algeo[1,3,4], Shucheng Xie[1*]

[1]*State Key Laboratory of Biogeology and Environmental Geology, and School of Earth Sciences, China University of Geosciences, Wuhan 430074, China*

[2]*School of Earth & Environment, University of Leeds, Leeds, LS2 9JT, UK*

[3] *State Key Laboratory of Geological Processes and Mineral Resources, China University of Geosciences, Wuhan 430074, China*

[4]*Department of Geosciences, University of Cincinnati, Cincinnati, Ohio 45221-0013, U.S.A.*

*****E-mail: gmluo@cug.edu.cn; xiecug@163.com

**ABSTRACT**

Although the trajectory of the marine mass extinction at the ~252-Ma Permian-Triassic (P-Tr) boundary has been well studied, details of the coeval collapse of terrestrial ecosystems remain murky. Here, we use hydrocarbon biomarker compositions and other geological records (i.e., organic carbon isotopes ($\delta^{13}C_{org}$), charcoal abundance, and Hg content) from a tropical peatland succession in southwestern China to reconstruct in detail the history of terrestrial ecosystem collapse during the P-Tr crisis. Our high-resolution hydrocarbon biomarker records reveal that this collapse proceeded in a stepwise manner with increasing intensity as the crisis unfolded. We recognize three discrete crisis stages: Stage I within the uppermost Xuanwei Formation and Stages

II and III within the lowermost Kayitou Formation. Stage I, the early crisis stage, is marked by a significant decline in terrestrial biomass (continuing into the later stages), as recorded by reduced $C_{29}$ steranes relative to total steranes and a concomitant reduction in the ratio of pristane to phytane (Pr/Ph). Stage II, the main crisis stage, records intensified soil erosion and sediment flux as revealed by rising dibenzofuran (DBF) content and high hopane/sterane ratios, the disappearance of coal seams, a sharp negative shift in $\delta^{13}C_{org}$, and peak concentrations of charcoal reflecting increased wildfire incidence. Stage III, the late crisis stage characterized by enhanced soil erosion, corresponds to peak values of Hg and Hg/TOC but no charcoal peak, suggesting intensified volcanism and a return to a humid climate. These stages closely follow temperature records, which show a stepwise rise during the crisis interval, implying that the deforestation process was strongly influenced by punctuated rises in temperature and/or its attendant effects (e.g., climate aridification). This P-Tr transition scenario suggests that global warming can trigger deforestation and reduce terrestrial carbon storage, thus serving as a positive climate feedback, with important implications for present-day climate change.

*Keywords*: hydrocarbons; biomarkers; soil erosion; charcoal; mercury; climate feedback

## 1. Introduction

The most severe mass extinction of the Phanerozoic occurred during the Permian-Triassic (P-Tr) transition, with estimates of >80% of marine species going extinct (e.g., Sepkoski, 1989; Fan et al., 2020). The severity of this extinction event in terrestrial ecosystems remains less well-documented owing to more limited preservation of fossil material and a more tenuous global correlation framework for continental successions (Visscher et al., 1996; Fielding et al., 2019;

Nowak et al., 2019; Feng et al., 2020a; Lucas, 2021). However, terrestrial ecosystems are major players in the global carbon cycle, accounting for ~50% of modern carbon fixation, and dominate biodiversity and hydrological cycling on land via the effects of tropical rainforests (Ciais et al., 2005). Therefore, in order to fully understand the response of the Earth system to the P-Tr mass extinction, it will be necessary to better document changes in terrestrial ecosystems during this critical time interval.

Terrestrial ecosystems are known to have undergone a major turnover during the P-Tr crisis (Sephton et al., 2005; Zhang et al., 2016; Chu et al., 2020; Xu et. al. 2022). The large-scale loss of woody plants resulted in along (~20-million-year) cessation of peat/coal accumulation (Retallack et al., 1996; Vajda et al., 2020). Based on the abrupt disappearance of coal-forming forests in tropical regions, terrestrial ecosystems are thought to have experienced a rapid collapse during the latest Permian (Shen et al., 2011; Chu et al., 2016, 2020; Xu et. al. 2022), which differs from the two-step extinction recorded in many marine sections (Xie et al., 2005; Yin et al., 2007; Luo et al., 2008; Song et al., 2013). However, this scenario has recently been challenged on the basis of pollen records (Nowak et al., 2019). Thus, an alternative approach is required to evaluate the nature, duration, and processes of the P-Tr biocrisis and its effects on terrestrial ecosystems.

Hydrocarbon biomarkers, which are mainly sourced from biotic cell membranes, have been shown to serve as valuable proxies for biocommunity composition and environmental conditions (Peters et al., 2005; Luo et al., 2019). For example, biological events in the marine realm (e.g., blooms of cyanobacteria and green sulfur bacteria) during the P-Tr mass extinction have been identified using hydrocarbon biomarkers (Grice et al., 2005; Xie et al., 2005). In addition, compared with plant macrofossils, hydrocarbon biomarkers are more abundant and less affected by preservation biases and, as a result, can provide higher-resolution temporal records.

Hyperwarming and oceanic anoxia were important features of the P-Tr crisis (Sun et al. 2012). Low-latitude sea-surface temperatures are estimated to have increased by more than 10 °C, reaching values as high as 35 °C in the earliest Triassic, according to oxygen isotope records of conodont apatite (Joachimski et al., 2012, 2019; Sun et al.,2012; Chen B et al., 2013; Schobben et al., 2014; Chen J et al., 2016; Shen et al., 2019). Hyperwarming reduced oxygen solubility in seawater and intensified oceanic stratification (Song et al., 2013), resulting in expanded oceanic anoxia that may have been a prime killing mechanism in marine environments (Wignall and Twitchett, 1996). How terrestrial carbon storage and primary productivity responded to this substantial rise in temperature remains an open question, although it represents a critical factor in evaluating feedbacks to global warming within terrestrial ecosystems (Ciais et al., 2005). Furthermore, this hyperwarming event appears to have played out in several stages, with an initial small increase preceding a catastrophic temperature rise (Joachimski et al., 2012; Shen et al., 2019). The more expanded temporal resolution offered by coeval terrestrial successions (Wu et al., 2020) may help to investigate the responses of terrestrial ecosystems to the temperature increase of different magnitudes.

In this study, we analyzed hydrocarbon biomarkers in a terrestrial P-Tr boundary succession in a drillcore (ZK4703) from southwestern China. We then integrated these records with published fossil-plant distribution, organic carbon isotope composition ($\delta^{13}C_{org}$), charcoal abundance, and Hg content data for the study core and/or study area, and compared these datasets to coeval marine crisis and tropical seawater temperature profiles. Our goals were to (1) delineate the trajectory of the tropical forest ecosystem crisis, as well as their correlations with the marine crisis, (2) draw inferences regarding the stresses on tropical forest ecosystems during the P-Tr crisis, focusing on temperature changes, and (3) evaluate these relationships in terms of climate-system feedbacks operating through the global carbon cycle. Our study provides fresh insights into changes in terrestrial ecosystems during the P-Tr crisis and their potential role in amplifying the crisis in marine ecosystems.

## 2. Geological background

The South China Craton was located in the eastern Paleo-Tethys Ocean, proximally to the paleo-Equator, during the P-Tr transition (Fig. 1). A series of P-Tr sections containing terrestrial, mixed, and marine facies crop out in the border region of eastern Yunnan and western Guizhou provinces (Fig. 1; Shen et al., 2011; Yin et al., 2014; Zhang et al., 2016, 2021). Core ZK4703 (25°32′29″N, 104°17′24″E) was drilled in Anzichong Village of Dahe Town, about 15 km south of Fuyuan County, Qujing City, Yunnan Province, South China, in an area dominated by terrestrial facies consisting of fluvial-alluvial-paludal deposits (Fig. 1).

In Core ZK4703, the P-Tr transition interval is contained within the upper Xuanwei and lower Kayitou formations (Chu et al., 2016; Zhang et al., 2016; Wignall et al., 2020). The Xuanwei Formation consists dominantly of mudstone and sandstone and has many coal seams and abundant plant fossils belonging to the *Gigantopteris* flora, which was characteristic of tropical rainforest-type vegetation during the Late Permian (Shen et al., 2011). The Kayitou Formation is lithologically similar but lacks coal seams and is shale dominated (Chu et al., 2020). Both the Xuanwei and Kayitou formations were deposited in muddy paralic conditions (Bercovici et al., 2015; Zhang et al., 2016; Chu et al., 2020; Wignall et al. 2020). The last fossils of *Gigantopteris*-type vegetation occur in the lowermost Kayitou Formation (Fig. 2; Zhang et al., 2016; Chu et al., 2020), a few centimeters above the last coal seam, which defines the Xuanwei/Kayitou formation contact, and which is associated with the sharp, negative shift in $\delta^{13}C_{org}$ that globally characterizes the interval between the main extinction horizon and the P-Tr boundary (Korte and Kozur, 2010). The top of the Xuanwei Formation was dated to 252.30 ± 0.07 Ma based on the zircon U-Pb age of a volcanic ash bed in the Chahe section in Guizhou Province, which is close to the absolute age of bed 25 (252.28 ± 0.08 Ma) in the Meishan section (Fig. 1; Shen et al., 2011).

Forty samples were collected from Core ZK4703 over a 27-m-thick stratigraphic interval representing ~200 kyr based on a duration of ~60 kyr duration (cf. Burgess et al., 2014) for the 9-m-thick crisis interval (see part 5.4). Thus, the sampling interval of our study achieves a temporal resolution of ~5 $kyr^{-1}$, which is significantly shorter than the estimated ~60 kyr duration of the marine mass extinction (Burgess et al., 2014). Our results for hydrocarbon biomarkers are paired with $\delta^{13}C_{org}$ and inorganic geochemical data generated by Chu et al. (2020) for the same sample suite.

## 3. Materials and methods

### *3.1. Sample preparation*

The glassware, glass wool, silica gel, and aluminum foil to be used for analysis of samples were baked at 500 °C for 8 h, and quartz sand was baked at 550 °C for >8 h to remove organic contaminants. Activated copper, used to sequester elemental sulfur, was cleaned by ultrasonication in methanol (MeOH) and dichloromethane (DCM) three times each after activation with hydrochloric acid (HCl). All solvents (*n*-hexane, DCM, and MeOH) used in sample extraction and equipment cleaning were of high-purity grade (OmniSolv, EMD Chemicals).

The procedures for rock sample processing and hydrocarbon biomarker extraction were adapted from those described in Luo et al. (2015). Firstly, the outside surfaces of core samples were trimmed away before sample processing, after which the core chips were cut into small pieces of about 1 $cm^3$ each. Secondly, all rock pieces were sequentially rinsed with DCM. Thirdly, after drying, the rock pieces were ground to a fine powder (<100 mesh) using a stainless-steel puck mill. Between samples, the puck mill was cleaned by grinding with baked quartz sand (at 550 °C for >8 h) three times, followed by sequential washing with tap and DI water (deionized water), as well as by rinsing with DCM multiple times. Before grinding a new sample, the last aliquot of baked quartz sand from the cleaned puck mill was collected and processed as a procedural blank.

*3.2. Extraction and separation of hydrocarbons*

Aliquots of ~40-100 g of powdered rock were extracted with a Dionex accelerated solvent extractor (ASE 150) using dichloromethane and methane (9:1 by vol.). Before each extraction, 5α(H),14β(H)-androstane (0.09643 mg/mL) and D-chrysene (0.046 mg/mL) were added as internal standards for the saturated and aromatic fractions, respectively. To each extract was added cleaned and active copper wire to remove elemental sulfur during rotating evaporation. The total lipid extracts were separated into saturated, aromatic, and polar fractions using silica-gel (activated at 150 °C for 6 h) column chromatography by sequential elution with *n*-hexane (one half column dead-volume), DCM: *n*-hexane (1:1, two dead-volumes) and MeOH (one dead-volume). The saturated and aromatic fractions were left to dry prior to instrumental analyses.

*3.3. Instrumental analyses*

The saturated hydrocarbon fractions were analyzed by a gas chromatograph (GC, Agilent 8890A) equipped with a flame ionization detector (FID) and a DB-5 capillary column (30 m × 0.25 mm i.d., 0.25 μm film thickness). Then, both the saturated and aromatic fractions were analyzed in full-scan mode by a GC-mass spectrometer (GC-MS, Agilent 7890A/5975C) equipped with a DB-5 MS capillary column (60 m × 0.25 mm i.d., 0.25 μm film thickness) using the same temperature program as the GC-FID, during which the oven temperature was programmed to rise from 70 to 310 °C at 3 °C $min^{-1}$ and then held at 310 °C for 35 min. A constant flow of helium (1 mL $min^{-1}$) was used as the carrier gas. Ionization in the MS was achieved at 70 eV and 250 °C, and the scan range was 50 to 550 Dalton. Samples, dissolved in hexane, were introduced to an Agilent 7890A GC through a PTV injector operated in splitless mode.

Steranes and hopanes of the saturated fractions were further analyzed by an Agilent 7890B/7000C GC-triple quadruple mass spectrometer (GC-MS/MS) in metastable reaction monitoring (MRM) mode. The GC was equipped with an HP-5 MS capillary column (30 m × 0.25 mm i.d., 0.25 μm film thickness), and the oven temperature was programmed from 60 to 150 °C at 10 °C $min^{-1}$, then to 315 °C at 3 °C $min^{-1}$, at which temperature it was held for 24 min. Helium was used as the carrier gas at a constant flow of 1 mL $min^{-1}$. The ion source was operated in EI mode at 250 °C, 70 eV ionization energy, and 8 kV accelerating voltage. Both the sample preparation and instrumental analyses were performed in the State Key Laboratory of Biogeology and Environmental Geology at China University of Geosciences (Wuhan).

The compounds were identified according to their mass spectra and elution times compared with published data. The ratios between different compounds were based on the areas of each peak, calibrated relative to the amount of the internal standard (5α(H),14β(H)-androstane).

## 4. Results

Diverse and abundant hydrocarbon biomarkers were detected in the saturated and aromatic fractions, including normal alkanes (*n*-alkane) ranging from $C_{13}$ to $C_{33}$, acyclic isoprenoids (mainly pristane (Pr) and phytane (Ph)), $C_{27}$-$C_{29}$ desmethylsteranes, $C_{27}$-$C_{35}$ 17α,21β-hopanes, and dibenzofuran (DBF) and their methylated homologues (see Supplementary Materials for details). In core ZK4703, the sterane fraction of all samples is dominated by $C_{29}$ homologues. The ratio of $C_{29}$ steranes to total $C_{27}$-$C_{29}$ steranes, termed $C_{29}$/STN, ranges from 38.2% to 75.8%, with an average of 54.3 ± 9.8% (*n* = 39, Fig. 2B). $C_{29}$/STN averages 67.3 ± 7.1% (*n* = 7) in the lower Xuanwei Formation (688.5-679 m) but declines to ~40% at the Xuanwei/Kayitou formation contact. $C_{29}$/STN increases to ~55% in the lowermost Kayitou Formation (674.75-672.5 m), then declines to ~45% (672-669.75 m) before stabilizing in the overlying strata (669.25-663 m) (Fig. 2B).

The Pr/Ph profile displays a variation trend similar to that of $C_{29}$/STN (Fig. 2C). Pr/Ph varies around 3.0 in the lower Xuanwei Formation but declines to ~0.5 in its upper part. In the lowermost ~2.5 m of the overlying Kayitou Formation, Pr/Ph increases slightly to ~1.5 but then declines again to ~0.5 (672-669.75 m) before stabilizing in the overlying strata (669.25-663 m) (Fig. 2C).

The TOC-normalized concentrations of dibenzofuran (DBF/TOC) vary around 103.7 ± 41.2 ng/g (*n* = 6, ranging from 44.7 ng/g to 160.6 ng/g) in the lower Xuanwei Formation before decreasing to 28.4 ± 37.8 ng/g (*n* = 4, ranging from 3.1 ng/g to 83.9 ng/g) in its uppermost part (Fig. 2D). Two peaks are observed in the lowermost 5 m of the Kayitou Formation, rising to ~300 ng/g at 674 m and to ~400 ng/g at 671 m, above which DBF/TOC declines sharply to ~9.6 ± 11.5 ng/g (*n* = 9, ranging from 0.1 ng/g to 30.2 ng/g except for an outlier) and then remains low (Fig. 2D).

The ratio of hopanoids to steroids (H/S, see the Supplementary Materials for calculation) varies from 1.2 to 21.4 (Fig. 2E). Overall, the H/S ratios are relatively stable in the Xuanwei and Kayitou formations, varying around 6.2 ± 2.5 (*n* = 12) and 4.4 ± 2.3 (*n* = 12), respectively. Two positive shifts are observed in the lowermost Kayitou Formation, the first marked by a rise to ~20 at 674 m, and the second by a rise to ~12 at 671 m (Fig. 2E).

## 5. Discussion

### *5.1. Syngenicity of hydrocarbon biomarkers*

Multiple lines of evidence suggest that the hydrocarbon biomarkers recovered from core ZK4703 record depositional conditions. The characteristics of the hydrocarbon biomarkers are consistent with their sedimentary facies, e.g., the predominance of $C_{29}$ desmethylsteranes (Huang and Meinschein, 1976; Nishimura and Koyama, 1977) and the hopane/sterane ratios are higher than typical Phanerozoic marine values of 0.5-2 (Peters et al., 2005). Second, similar thermal maturity indices are observed in bulk organic carbon and hydrocarbon extracts (Fig. 3A, B). With limited exceptions, the Rock-Eval pyrolysis analysis reveals that the maximum temperatures of the pyrolytic hydrocarbon peak $S_2$ ($T_{max}$) are around 454 °C, suggesting that the thermal maturity of this section is located in the upper oil window (Table S1). Meanwhile, isomerization at position C-22 in the $C_{31}$ homohopane side-chain, i.e., the ratio of 22S/(22S + 22R), is an excellent thermal maturity proxy, being around 58-60% in the main phase of petroleum generation (Peters et al., 2005). In core ZK4703, the average value of 22S/(S+R) of $C_{31}$ homohopanes is 59%, which is consistent with a thermal maturity in the upper oil window, as inferred from $T_{max}$ values (Fig. 3A). Similar thermal maturity indices are observed in the isomerization of steranes, e.g., αββ/(αββ+ααα) of $C_{29}$ steranes and 20S/(S+R) of $C_{29}$ ααα-steranes (Fig. 3B). The estimated thermal maturity is also supported by the distribution of long-chain *n*-alkanes; no odd-even predominance is observed. Third, the carbon-isotope compositions of all *n*-alkanes display variation trends similar to bulk organic carbon (unpublished data), precluding significant contamination during sample collection and processing. Lastly, the relationship of temporal variation in hydrocarbon biomarker parameters to geological and geochemical records provides convincing evidence that these hydrocarbon biomarkers are of primary origin. Therefore, we suggest that these hydrocarbon biomarkers record primary signals and thus can be used to reconstruct variations in terrestrial ecosystems in South China during the P-Tr transition.

### *5.2. Crisis of tropical forest ecosystems during the P-Tr transition*

Secular patterns of variation in multiple hydrocarbon biomarker proxies suggest that tropical forest ecosystems experienced a major crisis during the P-Tr transition. Specifically, the distribution of desmethylsteranes provides insights into eukaryotic community composition (Schwark and Empt, 2006). Terrestrial higher plants are generally dominated by $C_{29}$ steroids with smaller amounts of $C_{28}$ steroids and a lack of $C_{27}$ steroids, yielding high $C_{29}$/STN ratios (Huang and Meinschein, 1976), whereas aquatic phytoplankton are generally dominated by $C_{27}$ and $C_{28}$ steroids, yielding low $C_{29}$/STN ratios, although some green algae can synthesize a large fraction of $C_{29}$ steroids (Kodner et al., 2008). The Xuanwei Formation exhibits high $C_{29}$/STN ratios (67.3 ± 7.1%), consistent with terrestrial higher plants being the primary source of steroids. In the same interval, Pr/Ph ratios are high, varying around 3 (Fig. 2C). Multiple investigations have demonstrated that organic matter deposited in peat swamps is typically characterized by Pr/Ph > 2 (Peters et al., 2005; Xie et al., 2017). Therefore, the steroid and Pr/Ph proxies suggest that terrestrial higher plants were the primary source of organic matter to the Xuanwei Formation, which is consistent with its known macrofloral fossil content and abundant coal seams (Fig. 4). In contrast, the Kayitou Formation exhibits lower values of both $C_{29}$/STN and Pr/Ph, varying around 45% and 0.5, respectively (Fig. 2B, C). Since there is no associated sedimentary facies change at the level of the formation contact (Chu et al., 2020), the lower proxy values in the Kayitou Formation are indicative not of a change in environment but, rather, of a large decrease in the fraction of organic matter sourced from terrestrial higher plants. A similar decrease in Pr/Ph has been reported from approximately the same stratigraphic level of high paleo-latitude P-Tr boundary sections in India (Bhattacharya et al., 2021).

In addition, the background DBF/TOC values of the Xuanwei Formation (103.7 ± 41.2 ng/g; $n$ = 6) are higher than those of the Kayitou Formation (9.6 ± 11.5 ng/g; $n$ = 9). Furan-containing compounds, such as DBF, are mainly produced through microbially mediated dehydration of soil polysaccharides (Huang et al., 1998) or by the oxidative coupling of phenolic compounds in lignin derived from woody plants (Fenton et al., 2007). The enrichment of DBF and its methylated homologues generally points to a substantial increase in terrestrial organic matter enriched in lignin or soil polysaccharides, thus serving as a proxy for inputs from woody plants or massive soil erosion accompanying the destruction of land vegetation (Sephton et al., 2005; Fenton et al., 2007; Xie et al., 2007). The substantially lower background DBF/TOC values of the lower Kayitou Formation relative to those of the upper Xuanwei Formation are consistent with a large decrease in woody plant biomass after the end-Permian crisis, as high soil erosion rates (e.g., Sephton et al., 2005) would have increased DBF/TOC ratios, other factors being equal (see below).

In summary, multiple hydrocarbon proxies (i.e., $C_{29}$/STN, Pr/Ph, and DBF/TOC) show significant declines from the Xuanwei Formation to the Kayitou Formation. Thus, these records suggest that tropical forest ecosystems on the South China continent experienced a substantial crisis during the P-Tr transition, as also indicated by the disappearance of coal seams and higher plant fossils (Fig. 4).

*5.3. Stepwise deforestation during the P-Tr crisis*

Fossil plant diversity data generally suggest that the end-Permian crisis of tropical forest ecosystems was a rapid event that coincided with the termination of coal seam formation (Fig. 4). For example, compiled paleo-floral data for the Guanbachong, Chahe, Xiaohebian, Jiucaichong, Jinzhong and Jinjibang sections in southwestern China suggest that all major plant clades experienced a sudden extinction at the base of the Kayitou Formation, which is defined by the disappearance of coal seams (Fig. 4; Bercovici et al., 2015; Chu et al., 2016; Zhang et al., 2016; Feng et al., 2020a). However, the abundance of higher-plant macrofossils does not provide evidence for the history of deforestation.

The crisis interval reconstructed by the hydrocarbon biomarker records described above spans about 9 m in core ZK4703, including the uppermost 4 m of the Xuanwei Formation and the lowermost 5 m of the Kayitou Formation (Fig. 2). The onset of this interval predates the termination of coal seam deposition, the disappearance of the *Gigantopteris* flora, and the onset of the negative $\delta^{13}C_{org}$ shift, all of which coincide with the base of the Kayitou Formation. Thus, our high-resolution hydrocarbon biomarker records enable us to evaluate the events leading to the collapse of tropical rainforest-like ecosystems during the P-Tr mass extinction. Overall the crisis can be resolved into three stages: Stage I (Initial crisis), Stage II (Main crisis), and Stage III (Final crisis) (Figs. 2, 5).

Stage I (Initial Crisis), in the uppermost Xuanwei Formation, is characterized by significant declines in $C_{29}$/STN and Pr/Ph ratios, as well as in DBF/TOC (Fig. 2). As discussed above, these trends suggest a decrease in terrestrial higher-plant biomass. In addition, the lower DBF/TOC ratios in the uppermost Xuanwei Formation relative to Upper Permian background values indicate that there was little or no change in soil ecosystems at this point since such changes would have significantly increased the flux of DBF and related compounds (Sephton et al., 2005; Xie et al., 2007). This inference is indirectly supported by relatively constant H/S ratios which reflect in general the abundance of bacteria relative to the eukaryotic organisms (Peters et al., 2005), because an increase in nutrient flux accompanying a soil crisis would have stimulated marine prokaryotic bacterial productivity and, consequently, resulted in elevated H/S values (e.g., Cao et al., 2009; Rohrssen et al., 2013). Therefore, while the proportion of higher-plant biomass declined during Stage I, there was little to no change in soil communities at that time.

Stage II (Main crisis), in the lowermost 2.5 m of the Kayitou Formation, is characterized by a substantial increase in DBF/TOC, to values that are much higher than background values of the Xuanwei Formation (Fig. 2). This enrichment of DBF and its methylated homologues is consistent with a massive soil erosion event as terrestrial ecosystems collapsed (Sephton et al., 2005; Xie et al., 2007). This inference is supported by a concurrent large increase in H/S ratios, suggesting that an elevated nutrient flux linked to soil erosion promoted blooms of marine prokaryotic bacteria (Cao et al., 2009; Rohrssen et al., 2013). The declining trends in $C_{29}$/STN and Pr/Ph seen in Stage I ceased in Stage II when values increased slightly, although they remained lower than background values of the Xuanwei Formation (Fig. 2). In addition, enhanced soil erosion based on organic geochemistry has been reported from South China and Europe (e.g., Sephton et al., 2005; Wang et al., 2007; Xie et al., 2007), which is supported by the elevated sedimentation rate and claystone breccias observed in the earliest Triassic (Retallack, 2005; Algeo and Twitchett, 2010). Intriguingly, the beginning of Stage II coincided with the termination of coal deposition, the disappearance of the *Gigantopteris* flora, peak charcoal abundance, and the sharp negative shift in $\delta^{13}C_{org}$ (Fig. 2; Chu et al., 2020) that is ubiquitously present between the main extinction horizon and the P-Tr boundary (e.g., Korte and Kozur, 2010). Thus, Stage II represents the main terrestrial crisis.

Stage III (Final stage) of the terrestrial crisis is marked by another transient increase in DBF/TOC and H/S as well as declines in $C_{29}$/STN and Pr/Ph (Fig. 2). The paired decreases in $C_{29}$/STN and Pr/Ph suggest that terrestrial higher-plant biomass declined further, whereas the increases in DBF/TOC and H/S indicate further disturbance of soil ecosystems. This stage is also characterized by substantial increases in Hg/TOC, Cu/TOC, and malformed plant spores (Fig. 2; Chu et al., 2020, 2021). This last observation suggests that floras were generally stressed, with metal toxicity or damage from UV radiation as potential causes (Visscher et al., 2004; Chu et al., 2021). In addition, the high Hg/TOC values, which are commonly utilized as a marker for large-scale volcanic activity (e.g., Grasby et al., 2017), suggest that the trigger of this stage was volcanic in nature. In contrast to Stage II, charcoal abundance in Stage III is much lower (Fig. 2), which probably reflects a further decline in higher-plant (especially woody plant) biomass, although climate effects (e.g., increased humidity) cannot be ruled out.

*5.4. Correlations between the terrestrial and marine crises*

The hydrocarbon biomarker records of core ZK4703 presented here reconstruct the history of deforestation in rainforest-like ecosystems during the P-Tr transition in South China (Figs. 2, 5). The main crisis, marked by declining terrestrial biomass, enhanced soil erosion, the disappearance of woody plants, and peak concentrations of charcoal, coincided with the sharp negative shift in $\delta^{13}C_{org}$ (Shen et al., 2011; Chu et al., 2020). In the marine realm, the main mass extinction occurred simultaneously with a sharp negative shift in carbonate $\delta^{13}C$ (Xie et al., 2007; Korte and Kozur, 2010; Richoz et al., 2010). Assuming that the sharp negative shifts in terrestrial

$\delta^{13}C_{org}$ and marine $\delta^{13}C_{carb}$ were generated by the same mechanism, i.e., intensive volcanism (Burgess et al., 2017), then they must be correlative. In this context, the main crises in the terrestrial and marine realms are likely to have been coeval, or nearly so, as inferred in some earlier studies (Sephton et al., 2005; Shen et al., 2011).

Our hydrocarbon biomarker records identify an initial crisis (Stage I) preceding the main crisis that was characterized by a decrease in terrestrial higher plant biomass. This decrease was earlier than the main diversity losses among fossil plants and the shutdown of coal formation (Fig. 2). Intriguingly, this stage also preceded the sharp negative shift of C-isotopes associated with the latest Permian but coincided with a smaller, more gradual $\delta^{13}C_{org}$ decline in core ZK4703 (Fig. 2; Chu et al., 2020). A similar pattern is seen in marine sections, where a gradual decline of $\delta^{13}C_{carb}$ is typically present before an accelerated negative shift (e.g., Richoz et al., 2010). This initial shift in $\delta^{13}C_{carb}$ has been offered as evidence for a prelude crisis in marine environments, with effects especially evident among pelagic clades such as ammonites, radiolarians, and conodonts (Yin et al., 2007; Luo et al., 2008). Therefore, an initial crisis is evident in both the terrestrial and marine realms. However, the current temporal resolution is insufficient to determine if the initial crisis began first on land or in the sea, although some studies have proposed an earlier onset on land (Fielding et al., 2019; Chu et al., 2020).

Stage III in core ZK4703, which is characterized by elevated soil erosion and bloom of bacteria, corresponds to the second peak values of Hg/TOC (Fig. 2; Chu et al., 2020). Recent work on the same core shows that this stage also coincided with the peak value of Cu/TOC and malformed plant spores (Chu et al., 2021). Peaks of Hg/TOC, which are markers of extensive volcanic emissions (e.g., Grasby et al., 2017), suggest that Stage III corresponded to an interval of intensive volcanic activity. Intriguingly, in core ZK4703, the Stage III and the Hg/TOC peak are located above the sharp negative shift of $\delta^{13}C_{org}$, and coincide with the end of a gradual positive shift of $\delta^{13}C_{org}$ (Fig. 2). Similar temporal relationship between the Hg/TOC and $\delta^{13}C_{org}$ is also observed in the nearby Chinahe section (Chu et al., 2020). It is interesting to note that the second stage of mass extinction recognized in the marine realm occurred at the base of bed 28 in the Meishan section (Xie et al., 2005; Yin et al., 2007; Song et al., 2013). In the marine realm, the correlative interval corresponds to the end of a slight positive shift in $\delta^{13}C_{carb}$ and a layer of volcanic ash (Bed 28) (Yin et al., 2001; Xie et al., 2007). Therefore, we suggest that it is likely that Stage III observed in the terrestrial realm in South China might coincide with the second stage of mass extinction in the marine realm.

The (near-)synchronous crises in the terrestrial and marine realms suggest that both were responding to a common environmental forcing, i.e., temperature rise. However, it is also likely that these two ecosystems might be intimately interconnected, e.g., through continental weathering and nutrient fluxes (Algeo and Twitchett, 2010). The elevated nutrients flux accompanying terrestrial crisis and soil erosion would promote marine primary productivity and exacerbate marine anoxia (Mays et al., 2021; Wu et al., 2021), which might consequently amplify the crisis of marine ecosystems. Such inferences are supported by elevated bulk accumulation rates, increased clastic fluxes, and more radiogenic seawater strontium isotope compositions ($^{87}Sr/^{86}Sr$) (Algeo and Twitchett, 2010; Song et al., 2015). However, the nature and intensity of the links between the terrestrial and marine crises will require further investigation.

### *5.5. Environmental influences on the terrestrial crisis*

The marine biotic crisis has been widely attributed to expansion of oceanic anoxia, in some cases at depths sufficiently shallow to generate photic-zone euxinia (Grice et al., 2005; Xie et al., 2017). Although a decline in atmospheric $pO_2$ during the P-Tr transition has been inferred (Huey and Ward, 2005), it is unlikely to have been large enough to affect terrestrial ecosystems as most reconstructions suggest that the $pO_2$ were higher than 20% through the P-Tr transition (Krause et al., 2018 and references therein). More likely contributors to terrestrial ecosystem stress are effects linked to eruptions of the Siberian Traps Large Igneous Province (Black et al., 2014; Hochuli et al., 2017; Chu et al., 2021). For example, the high concentrations of spore tetrads and teratological pollen grains have been linked to air pollution and heavy metal contamination (Hochuli et al., 2017; Chu et al., 2021), and acid rain (Black et al., 2014). Enhanced UV radiation is also thought to have had harmful effects (Visscher et al., 2004; Liu et al., 2023). Since these effects were mainly brief, the cause-and-effect relationships between them and the long-term crisis of terrestrial ecosystems require further exploration.

In addition to the environmental factors listed above, a temperature rise is a long-term event that would have had substantial effects on terrestrial ecosystems. Significant progress has been achieved in the past decade in reconstructing secular temperature variation through the P-Tr transition. Variation of oxygen isotopes in conodont apatite has shown that low-latitude sea-surface temperatures increased by >10 °C and reached values as high as 35 °C during the P-Tr transition (Joachimski et al., 2012, 2019; Chen B et al., 2013; Schobben et al., 2014; Chen J et al., 2016; Shen et al., 2019). High-resolution stratigraphic data also reveal a temperature increase of 3 to 5 °C from a background temperature of about 24 °C directly before the main mass extinction (Joachimski et al., 2012; Shen et al., 2019). Using relationships between temperature and chemical index of alteration (CIA), Frank et al. (2021) proposed that there was a high-latitude terrestrial temperature increase of 10-14 °C from the latest Permian to the earliest Triassic on the southeastern margin of Gondwana, with the onset of warming during the late Lopingian, or somewhat before the main mass extinction.

The stages of the stepwise collapse of terrestrial ecosystems inferred here closely coincided with punctuated rises in marine temperature records (Fig. 2; Joachimski et al., 2012; Chen et al., 2013; Shen et al., 2019). The Stage I crisis coincided with the initial rise of ~3 to 5 °C (from ~24 to ~28 °C) in marine settings as well as with a rise in terrestrial temperatures (Frank et al., 2021). Present-day extreme temperature events are known to cause less efficient photosynthesis and decrease terrestrial primary productivity (Ciais et al., 2005), and the same phenomenon may have occurred during the Stage I crisis. As the temperatures reconstructed by conodont apatite are averages over a longtime interval (e.g., a few to hundreds of thousand years), brief heat waves cannot be observed in such geological records. According to climate models, it is likely that extreme heat waves might have accompanied this temperature rise (Meehl and Tebaldi, 2005; Schär et al., 2004). We hypothesized that the decrease in plants' primary productivity during Stage I was related to extreme heat waves (Benca et al., 2018). However, this stage did not substantially affect floral diversity and soil ecosystems (Chu et al., 2020; this study), which can be attributed to the limited duration of such heat waves.

Stage II coincided with a large and rapid increase in marine temperatures, as well as the sharp negative shift in $\delta^{13}C$ (Joachimski et al., 2012, 2019; Shen et al., 2019), recording major perturbations in both marine and terrestrial ecosystems (Figs. 2, 4). The main crisis also coincided with a peak in charcoal abundance, suggesting an increased frequency of wildfire (Fig. 2). The increased prevalence of wildfire was likely caused by intense arid intervals accompanying global warming and devegetation (Feng et al., 2020b; Song et al., 2022). A similar pattern of floral changes during the hyperwarming episode at the Paleocene-Eocene boundary also saw an increase in the abundance of charcoal in many locations (cf. Xie et al., 2022), which was attributed to a change in floral composition and the development of a more flammable plant community (Denis et al., 2017). Low sterane and Pr/Ph suggest the replacement of the tree-dominated *Gigantopteris* flora with one composed of smaller shrubs may have increased the propensity for wildfires in Stage II. However, this hypothesis does not explain the decline of charcoal abundance in Stage III, even though the same shrub flora persisted (Chu et al., 2020). Therefore, the main terrestrial mass extinction and soil ecosystem crisis may have been due primarily to higher temperatures and aridity events.

The concurrent increase of charcoal and loss of coal seams suggests that wildfire played a critical role in shaping earliest Triassic terrestrial ecosystems. High charcoal concentrations suggest that combustible fuel, e.g., dead or dying forests of higher plants, was still present during this stage. This inference is supported by biomarker records—specifically, the declines in $C_{29}$/STN and Pr/Ph that characterized Stage I ceased in Stage II, and values even increased slightly although they remained lower than background values in the Xuanwei Formation (Fig. 2). Increased wildfire incidence in conjunction with the loss of coal seams implies combustion of higher plants in a hot, dry climate that inhibited coal formation. The temporal coincidence between the peak in charcoal abundance and enhanced soil erosion (as proxied by DBFs) hints at the significant role of wildfires in the soil crisis.

During Stage III, tropical sea-surface temperatures rose to >35 °C and remained high until the Dienerian substage (Fig. 2; Joachimski et al., 2012; Sun et al., 2012). Thus, average land temperatures would have risen to comparably high levels. Under such conditions, photorespiration in $C_3$ plants would have exceeded photosynthesis, limiting plant growth (Black et al., 2014). Fossil plant records suggest that floras in this stage and overlying strata consist of a monotonous assemblage of small plants dominated by *Annalepis* and *Peltaspermum* (Fig. 4; Chu et al., 2020), and hydrocarbon biomarker records suggest that terrestrial floral biomass experienced a further decline (Fig. 2). The high Hg/TOC ratios during Stage III suggest that intensive volcanic eruption likely occurred, possibly large-scale felsic volcanism in the vicinity of the South China Craton (Zhao et al., 2019; Zhang et al., 2021). This is supported by the peak values of Cu/TOC and teratological spores and pollen observed at the same level (Chu et al., 2021). In contrast to Stage II, the charcoal abundance in Stage III is much lower (Fig. 2), which may reflect a return to a humid climate and/or a decline in plant biomass, especially a lack of woody plants.

### *5.5. Implications for future global warming*

Rising atmospheric $pCO_2$ has the potential to enhance terrestrial photosynthetic and carbon uptake rates, especially in the tropics, serving as an important negative feedback on global warming (Schimel et al., 2015; Zhu et al., 2016). However, the operation and magnitude of this feedback in response to further increases in $pCO_2$, which are crucial factors in simulating future climate change, remain uncertain (Cox et al., 2013). Reconstructed atmospheric $pCO_2$ before the P-Tr transition (~300-500 ppm) is indistinguishable from the modern level (~420 ppm) (Li et al., 2019). Thus, the response of terrestrial plants to temperature rise during the P-Tr crisis may provide insights into outcomes of future global warming. Our findings suggest that rising temperatures will eventually lead to terrestrial ecosystem collapse, a process that may be triggered by temperatures now reached during extreme heat waves (~35 °C). It is predicted that the frequency of severe heat waves will increase during the present century in response to global warming (Schär et al., 2004; Meehl and Tebaldi, 2005). The evidence from P-Tr sedimentary archives suggests that such heat waves would sharply reduce terrestrial productivity, with the ultimate consequence being the loss of most woody vegetation and the shutdown of peat formation. Thus, this factor must be considered in evaluating the role of terrestrial ecosystems in attenuation of future global warming.

## 6. Conclusions

Hydrocarbon biomarker records recovered from core ZK4703 in South China suggest that tropical rainforest-like ecosystems experienced a major crisis during the P-Tr transition. In combination with sedimentological and paleontological data, our high-temporal-resolution biomarker records allow a detailed reconstruction of the deforestation process. The terrestrial crisis proceeded in a stepwise manner of increasingly intensity. Stage I was characterized by a significant decrease in the biomass of higher plants prior to a sharp negative shift of $\delta^{13}C_{org}$. Stage II, which represents the main crisis, coincided with enhanced soil erosion and a sharp negative shift of $\delta^{13}C_{org}$, as well as with the termination of coal seam deposition, disappearance of the *Gigantopteris* flora, and peak charcoal concentrations. Stage III, the final stage, was marked by a further decrease in terrestrial biomass, another episode of soil erosion, and peak values of Hg/TOC, Cu/TOC, and teratological spores and pollen. High-resolution correlation suggests that the episodic crisis in the terrestrial realm was concurrent with that in the marine realm, reflecting the intimate coupling of these ecosystems. The P-Tr crisis can be attributed to a substantial rise in global temperatures, probably exacerbated locally by extreme heat waves and their climate consequences, e.g., aridification and widespread wildfire. Lastly, this P-Tr transition model suggests that the heat waves accompanying rising temperatures resulted in diminished terrestrial carbon storage, a positive climate feedback that needs to be correctly parameterized in models of present and future climate change.

## Acknowledgments

This research was funded by the National Natural Science Foundation of China (Grant no. 41821001, 42293290), and Strategic Priority Research Program of the Chinese Academy of Sciences (No. XDB26000000). Prof. Zhuo Feng at Yunnan University is thanked for his constructive comments.

## Appendix A. Supplementary data

Supplementary data to this article can be found online.

## References

Algeo, T.J., Twitchett, R.J., 2010. Anomalous Early Triassic sediment fluxes due to elevated weathering rates and their biological consequences. Geology 38(11), 1023-1026. https://doi:10.1130/g31203.1.

Benca, J.P., Duijnstee, I.A.P., Looy, C.V., 2018. UV-B-induced forest sterility: Implications of ozone shield failure in Earth's largest extinction. Sci. Adv. 4(2), e1700618. https://doi:10.1126/sciadv.1700618.

Bercovici, A., Cui, Y., Forel, M.B., Yu, J.X., Vajda, V., 2015. Terrestrial paleoenvironment characterization across the Permian-Triassic boundary in South China. J. Asian Earth Sci. 98, 225-246. https://doi:10.1016/j.jseaes.2014.11.016.

Bhattacharya, S., Ankit, Y., Murthy, S., Kushwaha, V., 2021. Biotic response to environmental shift during the Permian-Triassic transition: Assessment from organic geochemical proxies and palynomorphs in terrestrial sediments from Raniganj Sub-basin, India. Palaeogeogr. Palaeoclimatol. Palaeoecol. 576, 110483. https://doi:10.1016/j.palaeo.2021.110483.

Black, B.A., Lamarque, J.F., Shields, C.A., Elkins-Tanton, L.T., Kiehl, J.T., 2014. Acid rain and ozone depletion from pulsed Siberian Traps magmatism. Geology 42(1), 67-70. https://doi:10.1130/g34875.1.

Burgess, S.D., Bowring, S., Shen, S.Z., 2014. High-precision timeline for Earth's most severe extinction. Proc. Natl. Acad. Sci. U.S.A. 111(9), 3316-3321. https://doi:10.1073/pnas.1317692111.

Burgess, S.D., Muirhead, J.D., Bowring, S.A., 2017. Initial pulse of Siberian Traps sills as the trigger of the end-Permian mass extinction. Nat. Commun. 8, 164. https://doi:10.1038/s41467-017-00083-9.

Cao, C.Q., Love, G.D., Hays, L.E., Wang, W., Shen, S.Z., Summons, R.E., 2009. Biogeochemical evidence for euxinic oceans and ecological disturbance presaging the end-Permian mass extinction event. Earth Planet. Sci. Lett. 281(3-4), 188-201. https://doi:10.1016/j.epsl.2009.02.012.

Chen, B., Joachimski, M.M., Shen, S.Z., Lambert, L.L., Lai, X.L., Wang, X.D., Chen, J., Yuan, D.X., 2013. Permian ice volume and palaeoclimate history: Oxygen isotope proxies revisited. Gondwana Res. 24(1), 77-89. https://doi:10.1016/j.gr.2012.07.007.

Chen, J., Shen, S.Z., Li, X.H., Xu, Y.G., Joachimski, M.M., Bowring, S.A., Erwin, D.H., Yuan, D.X., Chen, B., Zhang, H., Wang, Y., Cao, C.Q., Zheng, Q.F., Mu, L., 2016. High-resolution SIMS oxygen isotope analysis on conodont apatite from South China and implications for the end-Permian mass extinction. Palaeogeogr. Palaeoclimatol. Palaeoecol. 448, 26-38. https://doi:10.1016/j.palaeo.2015.11.025.

Chu, D.L., Yu, J.X., Tong, J.N., Benton, M.J., Song, H.J., Huang, Y.F., Song, T., Tian, L., 2016. Biostratigraphic correlation and mass extinction during the Permian-Triassic transition in terrestrial-marine siliciclastic settings of South China. Glob. Planet. Change 146, 67-88. https://doi:10.1016/j.gloplacha.2016.09.009.

Chu, D.L., Grasby, S.E., Song, H.J., Dal Corso, J., Wang, Y., Mather, T.A., Wu, Y.Y., Song, H.Y., Shu, W.C., Tong, J.N., Wignall, P.B., 2020. Ecological disturbance in tropical peatlands prior to marine Permian-Triassic mass extinction. Geology 48(3), 288-292. https://doi:10.1130/g46631.1.

Chu, D.L., Dal Corso, J., Shu, W.C., Song, H.J., Wignall, P.B., Grasby, S.E., van de Schootbrugge, B., Zong, K.Q., Wu, Y.Y., Tong, J.N., 2021. Metal-induced stress in survivor plants following the end-Permian collapse of land ecosystems. Geology 49(6), 657-661. https://doi:10.1130/g48333.1.

Ciais, P., Reichstein, M., Viovy, N., Granier, A., Ogee, J., Allard, V., Aubinet, M., Buchmann, N., Bernhofer, C., Carrara, A., Chevallier, F., De Noblet, N., Friend, A.D., Friedlingstein, P., Grunwald, T., Heinesch, B., Keronen, P., Knohl, A., Krinner, G., Loustau, D., Manca, G., Matteucci, G., Miglietta, F., Ourcival, J.M., Papale, D., Pilegaard, K., Rambal, S., Seufert, G., Soussana, J.F., Sanz, M.J., Schulze, E.D., Vesala, T., Valentini, R., 2005. Europe-wide reduction in primary productivity caused by the heat and drought in 2003. Nature 437(7058), 529-533. https://doi:10.1038/nature03972.

Cox, P.M., Pearson, D., Booth, B.B., Friedlingstein, P., Huntingford, C., Jones, C.D., Luke, C.M., 2013. Sensitivity of tropical carbon to climate change constrained by carbon dioxide variability. Nature 494(7437), 341-344. https://doi:10.1038/nature11882.

Denis, E.H., Pedentchouk, N., Schouten, S., Pagani, M., Freeman, K.H., 2017. Fire and ecosystem change in the Arctic across the Paleocene-Eocene Thermal Maximum. Earth Planet. Sci. Lett. 467, 149-156. https://doi:10.1016/j.epsl.2017.03.021.

Fan, J.X., Shen, S.Z., Erwin, D.H., Sadler, P.M., MacLeod, N., Cheng, Q.M., Hou, X.D., Yang, J., Wang, X.D., Wang, Y., Zhang, H., Chen, X., Li, G.X., Zhang, Y.C., Shi, Y.K., Yuan, D.X., Chen, Q., Zhang, L.N., Li, C., Zhao, Y.Y., 2020. A high-resolution summary of Cambrian to Early Triassic marine invertebrate biodiversity. Science 367(6475), 272-277. https://doi:10.1126/science.aax4953.

Feng, Z., Wei, H.B., Guo, Y., He, X.Y., Sui, Q., Zhou, Y., Liu, H.Y., Gou, X.D., Lv, Y., 2020a. From rainforest to herbland: New insights into land plant responses to the end-Permian mass extinction. Earth Sci. Rev. 204, 103153. https://doi:10.1016/j.earscirev.2020.103153.

Feng, Z., Wei, H.B., Ye, R.H., Sui, Q., Gou, X.D., Guo, Y., Liu, L.J., Yang, S.L., 2020b. Latest Permian Peltasperm plant from southwest China and its paleoenvironmental implications. Front. Earth Sci. 8, 559430. https://doi:10.3389/feart.2020.559430.

Fenton, S., Grice, K., Twitchett, R., Bottcher, M., Looy, C., Nabbefeld, B., 2007. Changes in biomarker abundances and sulfur isotopes of pyrite across the Permian-Triassic (P/Tr) Schuchert Dal section (East Greenland). Earth Planet. Sci. Lett. 262(1-2), 230-239. https://doi:10.1016/j.epsl.2007.07.033.

Fielding, C.R., Frank, T.D., McLoughlin, S., Vajda, V., Mays, C., Tevyaw, A.P., Winguth, A., Winguth, C., Nicoll, R.S., Bocking, M., Crowley, J.L., 2019. Age and pattern of the southern high-latitude continental end-Permian extinction constrained by multiproxy analysis. Nat. Commun. 10, 385. https://doi:10.1038/s41467-018-07934-z.

Frank, T.D., Fielding, C.R., Winguth, A.M.E., Savatic, K., Tevyaw, A., Winguth, C., McLoughlin, S., Vajda, V., Mays, C., Nicoll, R., Bocking, M., Crowley, J.L., 2021. Pace, magnitude, and nature of terrestrial climate change through the end-Permian extinction in southeastern Gondwana. Geology 49(9), 1089-1095. https://doi:10.1130/g48795.1.

Grasby, S.E., Shen, W.J., Yin, R.S., Gleason, J.D., Blum, J.D., Lepak, R.F., Hurley, J.P., Beauchamp, B., 2017. Isotopic signatures of mercury contamination in latest Permian oceans. Geology 45(1), 55-58. https://doi:10.1130/g38487.1.

Grice, K., Cao, C.Q., Love, G.D., Bottcher, M.E., Twitchett, R.J., Grosjean, E., Summons, R.E., Turgeon, S.C., Dunning, W., Jin, Y.G., 2005. Photic zone euxinia during the Permian-Triassic superanoxic event. Science 307(5710), 706-709. https://doi:10.1126/science.1104323.

Huang, W.Y., Meinschein, W.G., 1976. Sterols as ecological indicators. Geochim. Cosmochim. Acta 43(5), 739-745. https://doi:10.1016/0016-7037(79)90257-6.

Huang, Y., Eglinton, G., Van der Hage, E.R.E., Boon, J.J., Bol, R., Ineson, P., 1998. Dissolved organic matter and its parent organic matter in grass upland soil horizons studied by analytical pyrolysis techniques. Eur. J. Soil Sci. 49(1), 1-15. https://doi:10.1046/j.1365-2389.1998.00141.x.

Hochuli, P.A., Schneebeli-Hermann, E., Mangerud, G., Bucher, H., 2017. Evidence for atmospheric pollution across the Permian-Triassic transition. Geology 45(12), 1123-1126. https://doi:10.1130/g39496.1.

Huey, R.B., Ward, P.D., 2005. Hypoxia, global warming, and terrestrial Late Permian extinctions. Science 308(5720), 398-401. https://10.1126/science.1108019.

Joachimski, M.M., Lai, X.L., Shen, S.Z., Jiang, H.S., Luo, G.M., Chen, B., Chen, J., Sun, Y.D., 2012. Climate warming in the latest Permian and the Permian-Triassic mass extinction. Geology 40(3), 195-198. https://doi:10.1130/g32707.1.

Joachimski, M.M., Alekseev, A.S., Grigoryan, A., Gatovsky, Y.A., 2019. Siberian Trap volcanism, global warming and the Permian-Triassic mass extinction: New insights from Armenian

Permian-Triassic sections. Geol. Soc. Am. Bull. 132(1-2), 427-443. https://doi:10.1130/b35108.1.

Kodner, R.B., Pearson, A., Summons, R.E., Knoll, A.H., 2008. Sterols in red and green algae: quantification, phylogeny, and relevance for the interpretation of geologic steranes. Geobiology 6(4), 411-420. https://doi:10.1111/j.1472-4669.2008.00167.x.

Korte, C., Kozur, H.W., 2010. Carbon-isotope stratigraphy across the Permian-Triassic boundary: a review. J. Asian Earth Sci. 39(4), 215-235. https://doi:10.1016/j.jseaes.2010.01.005.

Krause, A.J., Mills, B.J.W., Zhang, S., Planavsky, N.J., Lenton, T.M., Poulton, S.W., 2018. Stepwise oxygenation of the Paleozoic atmosphere. Nat Commun. 9, 4081. https://doi:10.1038/s41467-018-06383-y.

Li, H., Yu, J.X., McElwain, J.C., Yiotis, C., Chen, Z.Q., 2019. Reconstruction of atmospheric $CO_2$ concentration during the late Changhsingian based on fossil conifers from the Dalong Formation in South China. Palaeogeogr. Palaeoclimatol. Palaeoecol. 519, 37-48. https://doi:10.1016/j.palaeo.2018.09.006.

Liu, F., Peng, H.P., Marshall, J.E.A., Lomax, B.H., Bomfleur, B., Kent, M.S., Fraser, W.T., Jardine, P., 2023. Dying in the Sun: Direct evidence for elevated UV-B radiation at the end-Permian mass extinction. Sci. Adv. 9(1), eabo6102. https://doi:10.1126/sciadv.abo6102.

Lucas, S.G., 2021. Nonmarine mass extinctions. Paleontol. Res. 25(4), 329-344. https://doi:10.2517/2021pr004.

Luo, G.M., Lai, X.L., Shi, G.R., Jiang, H.S., Yin, H.F., Xie, S.C., Tong, J.N., Zhang, K.X., He, W.H., Wignall, P.B., 2008. Size variation of conodont elements of the *Hindeodus-Isarcicella* clade during the Permian-Triassic transition in South China and its implication for mass extinction. Palaeogeogr. Palaeoclimatol. Palaeoecol. 264(1-2), 176-187. https://doi:10.1016/j.palaeo.2008.04.015.

Luo, G.M., Hallmann, C., Xie, S.C., Ruan, X.Y., Summons, R.E., 2015. Comparative microbial diversity and redox environments of black shale and stromatolite facies in the Mesoproterozoic Xiamaling Formation. Geochim. Cosmochim. Acta 151, 150-167. https://doi:10.1016/j.gca.2014.12.022.

Luo, G.M., Yang, H., Algeo, T.J., Hallmann, C., Xie, S.C., 2019. Lipid biomarkers for the reconstruction of deep-time environmental conditions. Earth Sci. Rev. 189, 99-124. https://doi:10.1016/j.earscirev.2018.03.005.

Mays, C., McLoughlin, S., Frank, T.D., Fielding, C.R., Slater, S.M., Vajda, V., 2021. Lethal microbial blooms delayed freshwater ecosystem recovery following the end-Permian extinction. Nat. Commun. 12, 5511. https://doi:10.1038/s41467-021-25711-3.

Meehl, G.A., Arblaster, J.M., Tebaldi, C., 2005. Understanding future patterns of increased precipitation intensity in climate model simulations. Geophys. Res. Lett. 32(18), L18719. https://doi:10.1029/2005gl023680.

Nishimura, M., Koyama, T., 1977. The occurrence of stanols in various living organisms and the behavior of sterols in contemporary sediments. Geochim. Cosmochim. Acta 41(3), 379-385. https://doi:10.1016/0016-7037(77)90265-4.

Nowak, H., Schneebeli-Hermann, E., Kustatscher, E., 2019. No mass extinction for land plants at the Permian-Triassic transition. Nat. Commun. 10, 384. https://doi:10.1038/s41467-018-07945-w.

Peters, K.E., Walters, C.C., Moldowan, J.M., 2005. The Biomarker Guide: Biomarkers and Isotopes in the Environment and Human History, 2nd ed. Cambridge University Press, Cambridge.

Retallack, G.J., Veevers, J.J., Morante, R., 1996. Global coal gap between Permian-Triassic extinction and Middle Triassic recovery of peat-forming plants. Geol. Soc. Am. Bull. 108(2), 195-207. https://doi:110.1130/0016-7606(1996)1082.3.CO;2.

Retallack, G.J., 2005. Early Triassic claystone breccias and soil-erosion crisis. J. Sediment. Res. 75(4), 679-695. https://doi.org/10.2110/jsr.2005.055.

Richoz, S., Krystyn, L., Baud, A., Brandner, R., Horacek, M., Mohtat-Aghai, P., 2010. Permian-Triassic boundary interval in the Middle East (Iran and N. Oman): Progressive environmental change from detailed carbonate carbon isotope marine curve and sedimentary evolution. J. Asian Earth Sci. 39(4), 236-253. https://doi:10.1016/j.jseaes.2009.12.014.

Rohrssen, M., Love, G.D., Fischer, W., Finnegan, S., Fike, D.A., 2013. Lipid biomarkers record fundamental changes in the microbial community structure of tropical seas during the Late Ordovician Hirnantian glaciation. Geology 41(2), 127-130. https://doi:10.1130/g33671.1.

Schär, C., Vidale, P.L., Luthi, D., Frei, C., Haberli, C., Liniger, M.A., Appenzeller, C., 2004. The role of increasing temperature variability in European summer heatwaves. Nature 427(6972), 332-336. https://doi:10.1038/nature02300.

Schimel, D., Pavlick, R., Fisher, J.B., Asner, G.P., Saatchi, S., Townsend, P., Miller, C., Frankenberg, C., Hibbard, K., Cox, P., 2015. Observing terrestrial ecosystems and the carbon cycle from space. Glob. Chang Biol. 21(5), 1762-1776. https://doi:10.1111/gcb.12822.

Schobben, M., Joachimski, M.M., Korn, D., Leda, L., Korte, C., 2014. Palaeotethys seawater temperature rise and an intensified hydrological cycle following the end-Permian mass extinction. Gondwana Res. 26(2), 675-683. https://doi:10.1016/j.gr.2013.07.019.

Schwark, L., Empt, P., 2006. Sterane biomarkers as indicators of Palaeozoicalgal evolution and extinction events. Palaeogeogr. Palaeoclimatol. Palaeoecol. 240(1-2), 225-236. https://doi:10.1016/j.palaeo.2006.03.050.

Sephton, M.A., Looy, C.V., Brinkhuis, H., Wignall, P.B., de Leeuw, J.W., Visscher, H., 2005. Catastrophic soil erosion during the end-Permian biotic crisis. Geology 33(12), 941-944. https://doi:10.1130/g21784.1.

Sepkoski, J.J., Jr., 1989. Periodicity in extinction and the problem of catastrophism in the history of life. J. Geol. Soc. London 146, 7-19. https://doi:10.1144/gsjgs.146.1.0007.

Shen, S.Z., Crowley, J.L., Wang, Y., Bowring, S.A., Erwin, D.H., Sadler, P.M., Cao, C.Q., Rothman, D.H., Henderson, C.M., Ramezani, J., Zhang, H., Shen, Y.N., Wang, X.D., Wang, W., Mu, L., Li, W.Z., Tang, Y.G., Liu, X.L., Liu, L.J., Zeng, Y., Jiang, Y.F., Jin, Y.G., 2011. Calibrating the end-Permian mass extinction. Science 334(6061), 1367-1372. https://doi:10.1126/science.1213454.

Shen, S.Z., Ramezani, J., Chen, J., Cao, C.Q., Erwin, D.H., Zhang, H., Xiang, L., Schoepfer, S.D., Henderson, C.M., Zheng, Q.F., Bowring, S.A., Wang, Y., Li, X.H., Wang, X.D., Yuan, D.X., Zhang, Y.C., Mu, L., Wang, J., Wu, Y.S., 2019. A sudden end-Permian mass extinction in South China. Geol. Soc. Am. Bull. 131(1-2), 205-223. https://doi:10.1130/b31909.1.

Song, H.J., Wignall, P.B., Tong, J.N., Yin, H.F., 2013. Two pulses of extinction during the Permian-Triassic crisis. Nat. Geosci. 6, 52-56. https://doi:10.1038/ngeo1649.

Song, H.J., Wignall, P.B., Tong, J.N., Song, H.Y., Chen, J., Chu, D.L., Tian, L., Luo, M., Zong, K.Q., Chen, Y.L., Lai, X.L., Zhang, K.X., Wang, H.M., 2015. Integrated Sr isotope variations and global environmental changes through the Late Permian to early Late Triassic. Earth Planet. Sci. Lett. 424, 140-147. https://doi:10.1016/j.epsl.2015.05.035.

Song, H.Y., Tong, J.N., Algeo, T.J., Horacek, M., Qiu, H., Song, H.J., Tian, L., Chen, Z.Q., 2013. Large vertical $\delta^{13}C_{DIC}$ gradients in Early Triassic seas of the South China craton: Implications for oceanographic changes related to Siberian Traps volcanism. Glob. Planet. Change 105, 7-20. https://10.1016/j.gloplacha.2012.10.023.

Song, Y., Tian, Y., Yu, J.X., Algeo, T.J., Luo, G.M., Chu, D.L., Xie, S.C., 2022. Wildfire response to rapid climate change during the Permian-Triassic biotic crisis. Glob. Planet. Change 215, 103872. https://10.1016/j.gloplacha.2022.103872.

Sun, Y.D., Joachimski, M.M., Wignall, P.B., Yan, C.B., Chen, Y.L., Jiang, H.S., Wang, L., Lai, X.L., 2012. Lethally hot temperatures during the Early Triassic greenhouse. Science 338(6105), 366-370. https://doi:10.1126/science.1224126.

Vajda, V., McLoughlin, S., Mays, C., Frank, T.D., Fielding, C.R., Tevyaw, A., Lehsten, V., Bocking, M., Nicoll, R.S., 2020. End-Permian (252 Mya) deforestation, wildfires and flooding—An ancient biotic crisis with lessons for the present. Earth Planet. Sci. Lett. 529, 115875. https://doi:10.1016/j.epsl.2019.115875.

Visscher, H., Brinkhuis, H., Dilcher, D.L., Elsik, W.C., Eshet, Y., Looy, C.V., Rampino, M.R., Traverse, A., 1996. The terminal Paleozoic fungal event: Evidence of terrestrial ecosystem destabilization and collapse. Proc. Natl. Acad. Sci. U.S.A. 93(5), 2155-2158. https://doi:10.1073/pnas.93.5.2155.

Visscher, H., Looy, C.V., Collinson, M.E., Brinkhuis, H., Cittert, J., Kurschner, W.M., Sephton, M.A., 2004. Environmental mutagenesis during the end-Permian ecological crisis. Proc. Natl. Acad. Sci. U.S.A. 101(35), 12952-12956. https://doi:10.1073/pnas.0404472101.

Wignall, P.B., Twitchett, R.J., 1996. Oceanic anoxia and the end Permian mass extinction. Science 272, 1155-1158. https://10.1126/science.272.5265.1155.

Wignall, P.B., Chu, D.L., Hilton, J.M., Corso, J.D., Wu, Y.Y., Wang, Y., Atkinson, J., Tong, J.N., 2020. Death in the shallows: The record of Permo-Triassic mass extinction in paralic settings, southwest China. Glob. Planet. Change 189, 103176. https://doi:10.1016/j.gloplacha.2020.103176.

Wu, B.J., Luo, G.M., Joachimski, M.M., Wignall, P.B., Lei, L.D., Huang, J.H., Lai, X.L., 2021. Carbon and nitrogen isotope evidence for widespread presence of anoxic intermediate waters before and during the Permian-Triassic mass extinction. Geol. Soc. Am. Bull. 134(5-6), 1397-1413. https://doi:10.1130/b36005.1.

Wu, Y.Y., Tong, J.N., Algeo, T.J., Chu, D.L., Cui, Y., Song, H.Y., Shu, W.C., Du, Y., 2020. Organic carbon isotopes in terrestrial Permian-Triassic boundary sections of North China: Implications for global carbon cycle perturbations. Geol. Soc. Am. Bull. 132(5-6), 1106-1118. https://doi:10.1130/B35228.1.

Wu, Y.Y., Chu, D.L., Tong, J.N., Song, H.J., Dal Corso, J., Wignall, P.B., Song, H.Y., Du, Y., Cui, Y., 2021. Six-fold increase of atmospheric $p\mathrm{CO_2}$ during the Permian-Triassic mass extinction. Nat. Commun. 12, 2137. https://doi:10.1038/s41467-021-22298-7.

Xie, S.C., Pancost, R.D., Yin, H.F., Wang, H.M, Evershed, R.P., 2005. Two episodes of microbial change coupled with Permo/Triassic faunal mass extinction. Nature 434(7032), 494-497. https://doi:10.1038/nature03396.

Xie, S.C., Pancost, R.D., Huang, J.H., Wignall, P.B., Yu, J.X., Tang, X.Y., Chen, L., Huang, X.Y., Lai, X.L., 2007. Changes in the global carbon cycle occurred as two episodes during the Permian-Triassic crisis. Geology 35(12), 1083-1086. https://doi:10.1130/g24224a.1.

Xie, S.C., Algeo, T.J., Zhou, W.F., Ruan, X.Y., Luo, G.M., Huang, J.H., Yan, J.X., 2017. Contrasting microbial community changes during mass extinctions at the Middle/Late Permian and Permian/Triassic boundaries. Earth Planet. Sci. Lett. 460, 180-191. https://doi:10.1016/j.epsl.2016.12.015.

Xie, Y.L., Wu, F.L., Fang, X.M., 2022. Abrupt collapse of a swamp ecosystem in northeast China during the Paleocene-Eocene Thermal Maximum. Palaeogeogr. Palaeoclimatol. Palaeoecol. 595, 110975. https://doi:10.1016/j.palaeo.2022.110975.

Xu, Z., Hilton, J., Yu, J.X., Wignall, P.B., Yin, H.F., Xue, Q., Ran, W.J., Li, H., Shen, J., Meng, F.S., 2022. End Permian to Middle Triassic plant species richness and abundance patterns in. South China: Coevolution of plants and the environment through the Permian-Triassic transition. Earth Sci. Rev. 232, 104136. https://10.1016/j.earscirev.2022.104136.

Yin, H.F., Zhang, K.X., Tong, J.N., Yang, Z.Y., Wu, S.B., 2001. The Global Stratotype Section and Point (GSSP) of the Permian-Triassic Boundary. Episodes 24(2), 102-114.

Yin, H.F., Feng, Q.L., Baud, A., Xie, S.C., Benton, M.J., Lai, X.L., Bottjer, D.J., 2007. The prelude of the end-Permian mass extinction predates a postulated bolide impact. Int. J. Earth Sci. 96, 903-909. https://doi:10.1007/s00531-006-0135-1.

Yin, H.F., Jiang, H.S., Xia, W.C., Feng, Q.L., Zhang, N., Shen, J., 2014. The end-Permian regression in South China and its implication on mass extinction. Earth Sci. Rev. 137, 19-33. https://doi:10.1016/j.earscirev.2013.06.003.

Zhang, H., Cao, C.Q., Liu, X.L., Mu, L., Zheng, Q.F., Liu, F., Xiang, L., Liu, L.J., Shen, S.Z., 2016. The terrestrial end-Permian mass extinction in South China. Palaeogeogr. Palaeoclimatol. Palaeoecol. 448, 108-124. https://doi:10.1016/j.palaeo.2015.07.002.

Zhang, H., Zhang, F.F., Chen, J.B., Erwin, D.H., Syverson, D.D., Ni, P., Rampino, M., Chi, Z., Cai, Y.F., Xiang, L., Li, W.Q., Liu, S.A., Wang, R.C., Wang, X.D., Feng, Z., Li, H.M., Zhang, T., Cai, H.M., Zheng, W., Cui, Y., Zhu, X.K., Hou, Z.Q., Wu, F.Y., Xu, Y.G., Planavsky, N., Shen, S.Z., 2021. Felsic volcanism as a factor driving the end-Permian mass extinction. Sci. Adv. 7(47), eabh1390. https://doi:10.1126/sciadv.abh1390.

Zhao, T., Algeo, T.J., Feng, Q., Zi, J.W., Xu, G., 2019. Tracing the provenance of volcanic ash in Permian-Triassic boundary strata, South China: Constraints from inherited and syn-depositional magmatic zircons. Palaeogeogr. Palaeoclimatol. Palaeoecol. 516, 190-202. https://doi:10.1016/j.palaeo.2018.12.002.

Zhu, Z.C., Piao, S.L., Myneni, R.B., Huang, M.T., Zeng, Z.Z., Canadell, J.G., Ciais, P., Sitch, S., Friedlingstein, P., Arneth, A., Cao, C.X., Cheng, L., Kato, E., Koven, C., Li, Y., Lian, X., Liu, Y.W., Liu, R.G., Mao, J.F., Pan, Y.Z., Peng, S.S., Peñuelas, J., Poulter, B., Pugh, T.A.M., Stocker, B.D., Viovy, N., Wang, X.H., Wang, Y.P., Xiao, Z.Q., Yang, H., Zaehle, S., Zeng, N., 2016. Greening of the Earth and its drivers. Nat. Clim. Change 6(8), 791-795. https://doi:10.1038/nclimate3004.

## Figure Captions

**Fig. 1.** Location of the study area. A: Global paleogeography reconstruction during the P-Tr transition. Base map courtesy of Ron Blakey (http://jan.ucc.nau.edu/~rcb7/). The red rectangle

represents area of map B. B: Simplified paleogeography of the South China (Chu et al., 2020) Craton showing the location of study core ZK4703 (red asterisk). Eq: paleo-Equator.

**Fig. 2.** Litho- and chemostratigraphy of core ZK4703 through the P-Tr transition. $C_{29}$/STN: ratio of $C_{29}$ steranes to the sum of $C_{27}$, $C_{28}$, and $C_{29}$ steranes; Pr: pristane; Ph: phytane; H: αβ-hopanes; S: desmethylsteranes; DBF: dibenzofuran. I-III: Crisis Stages I to III defined in this study. TOC (total organic carbon), $\delta^{13}C_{org}$, and Hg data are from Chu et al. (2020); marine temperature data are from Joachimski et al. (2012) and Chen B et al. (2013).

**Fig. 3.** Thermal maturity assessment based on isomerization of hopanes and steranes. (A) $C_{31}$ H 22S/(S+R) vs $C_{29}$-St ααα 20S/(S+R); (B) $C_{29}$-St ααα 20S/(S+R) vs $C_{29}$-St αββ/(αββ+ααα). Data sources are listed in Table S1.

**Fig. 4.** The diversity of plant fossil distribution and other environmental perturbations through the P-Tr transition. Carbon isotope ($\delta^{13}C$) and TOC sources: Chahe from Shen et al. (2011); ZK4703 and Chinahe from Chu et al. (2020); and Jiucaichong from Wu et al. (2021). Marine temperature data are from Joachimski et al. (2012) and Chen B et al. (2013). Plant fossil distributions are based on study of six terrestrial sections in southwestern China by Chu et al. (2016).

**Fig. 5.** Reconstructed deforestation process of a tropical rainforest-like ecosystem during the P-Tr transition. The five panels correspond to the intervals of Fig. 2: Pre-Crisis, Crisis Stages I to III, and Post-Crisis. Crisis Stage I was marked by a large decline in the terrestrial biomass, Stage II by a high incidence of wildfire, and Stage III by intensified volcanism and a possible return to a humid climate. Recovery of tree plants occurred mainly in the Post-Crisis interval. See the text for details.

## FIGURES AND FIGURE CAPTIONS

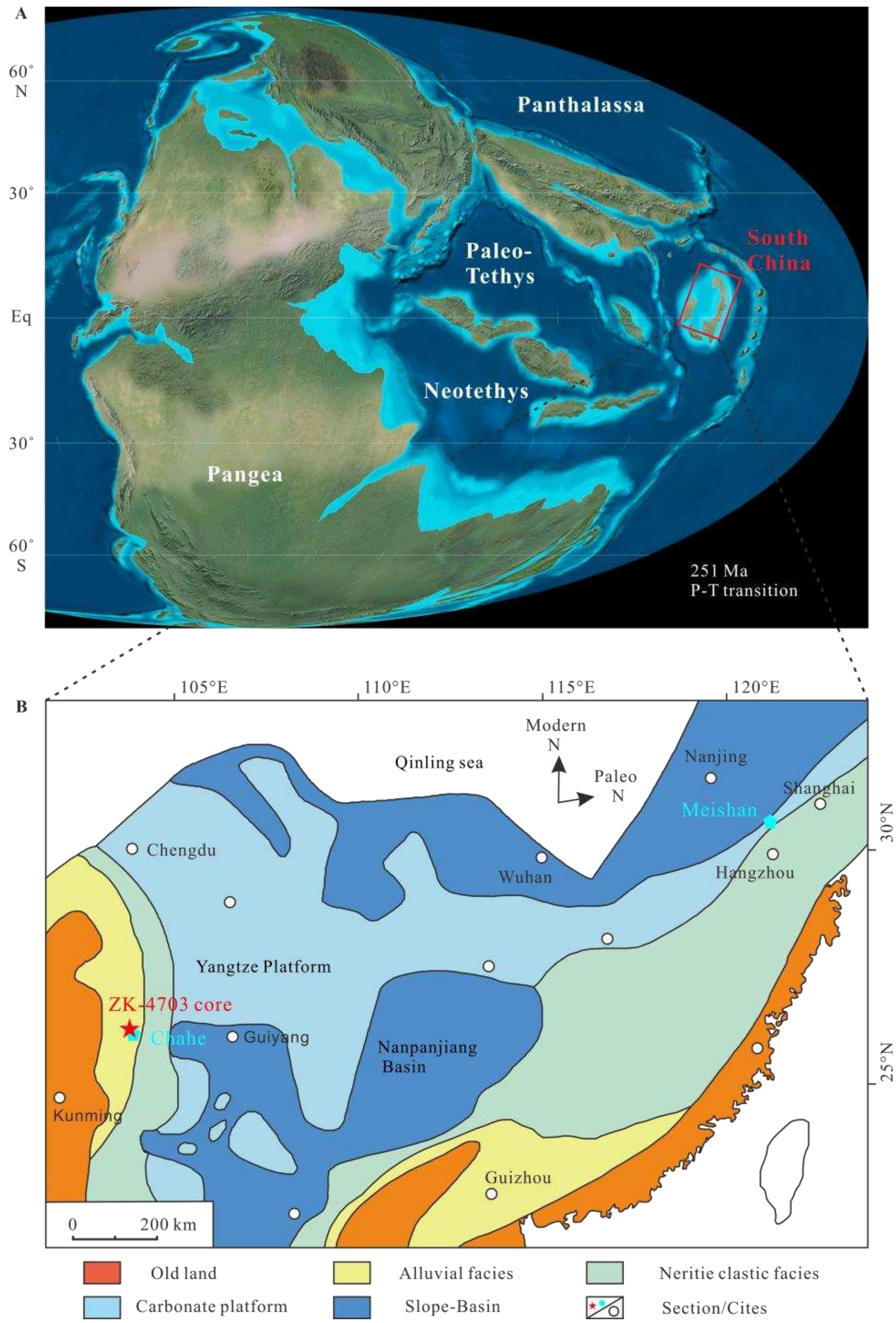


**Fig. 1.** Location of the study area. A: Global paleogeography reconstruction during the P-Tr transition. Base map courtesy of Ron Blakey (http://jan.ucc.nau.edu/~rcb7/). The red rectangle represents area of map B. B: Simplified paleogeography of the South China

(Chu et al., 2020) Craton showing the location of study core ZK4703 (red asterisk). Eq: paleo-Equator.

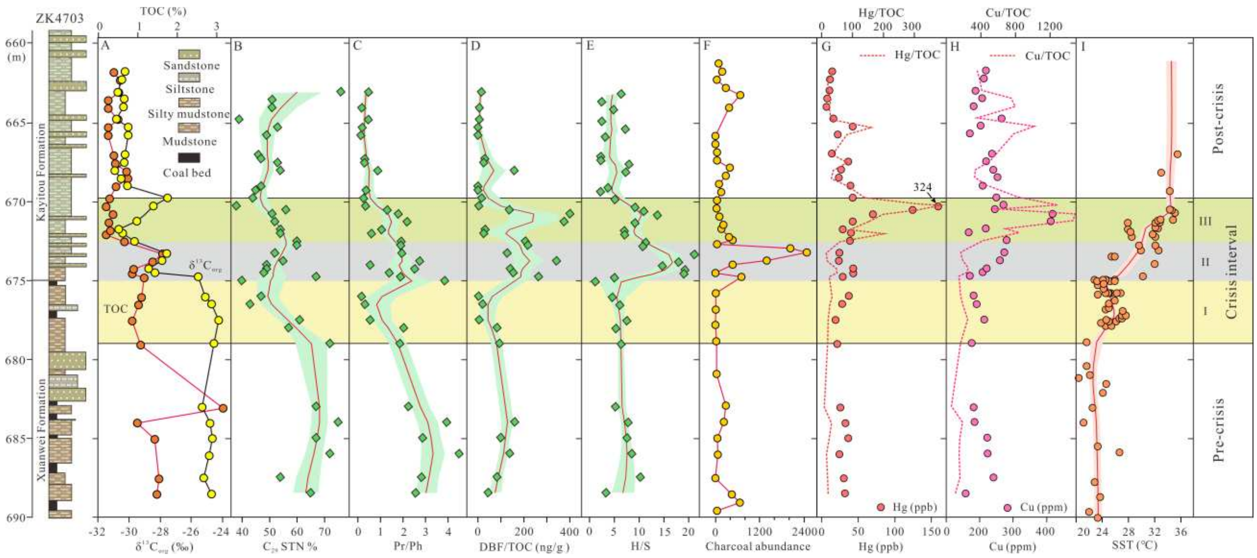


**Fig. 2.** Litho- and chemostratigraphy of core ZK4703 through the P-Tr transition. $C_{29}$/STN: ratio of $C_{29}$ steranes to the sum of $C_{27}$, $C_{28}$, and $C_{29}$ steranes; Pr: pristane; Ph: phytane; H: αβ-hopanes; S: desmethylsteranes; DBF: dibenzofuran. I-III: Crisis Stages I to III defined in this study. TOC (total organic carbon), $\delta^{13}C_{org}$, and Hg data are from Chu et al. (2020); marine temperature data are from Joachimski et al. (2012) and Chen B et al. (2013).

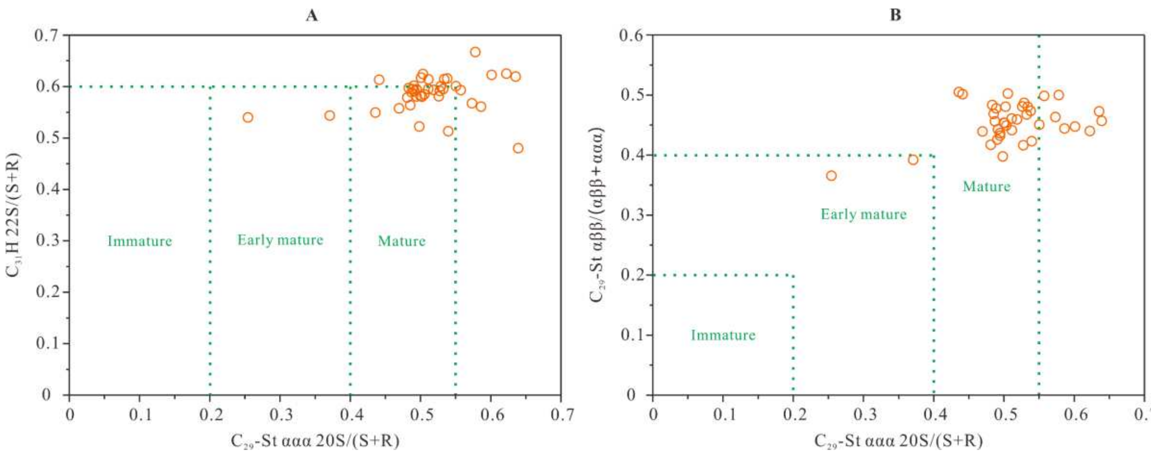


**Fig. 3.** Thermal maturity assessment based on isomerization of hopanes and steranes. (A) $C_{31}$ H 22S/(S+R) vs $C_{29}$-St ααα 20S/(S+R); (B) $C_{29}$-St ααα 20S/(S+R) vs $C_{29}$-St αββ/(αββ+ααα). Data sources are listed in Table S1.

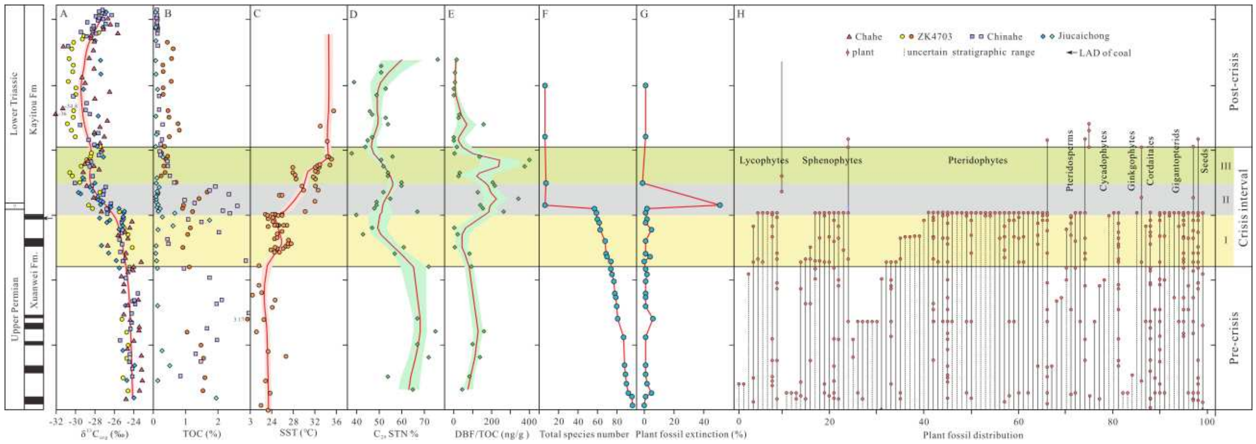

**Fig. 4.** The diversity of plant fossil distribution and other environmental perturbations through the P-Tr transition. Carbon isotope ($\delta^{13}C$) and TOC sources: Chahe from Shen et al. (2011); ZK4703 and Chinahe from Chu et al. (2020); and Jiucaichong from Wu et al. (2021). Marine temperature data are from Joachimski et al. (2012) and Chen B et al. (2013). Plant fossil distributions are based on study of six terrestrial sections in southwestern China by Chu et al. (2016).

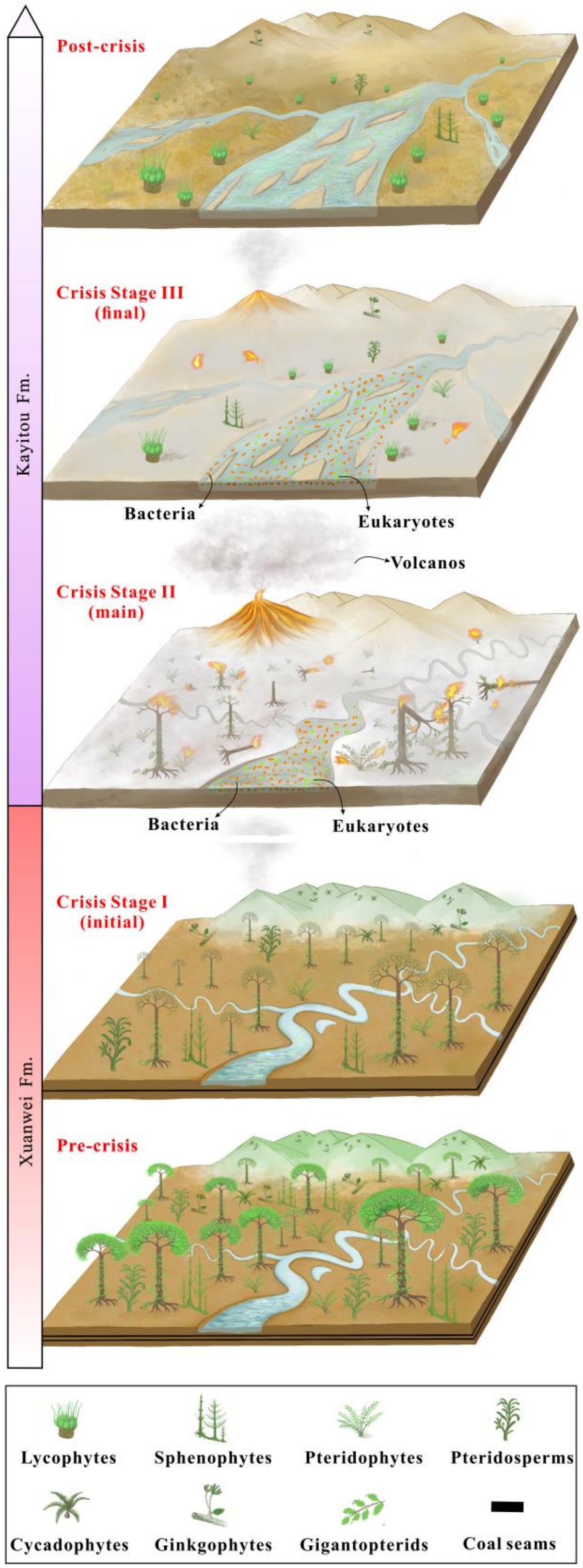


**Fig. 5.** Reconstructed deforestation process of a tropical rainforest-like ecosystem during the P-Tr transition. The five panels correspond to the intervals of Fig. 2: Pre-Crisis, Crisis Stages I to III,

and Post-Crisis. Crisis Stage I was marked by a large decline in the terrestrial biomass, Stage II by a high incidence of wildfire, and Stage III by intensified volcanism and a possible return to a humid climate. Recovery of tree plants occurred mainly in the Post-Crisis interval. See the text for details.